A&A 541, A65 (2012)
DOI: 10.1051/0004-6361/201016261

Astronomy & Astrophysics

Herschel-PACS far-infrared detections of Lyman-α emitters at $2.0 \lesssim z \lesssim 3.5$[⋆,⋆⋆]

I. Oteo[1,2], A. Bongiovanni[1,2], A. M. Pérez García[1,2], J. Cepa[2,1], A. Ederoclite[1,2], M. Sánchez-Portal[3], I. Pintos-Castro[1,2], R. Pérez-Martínez[4], S. Berta[5], B. Magnelli[5], P. Popesso[5], F. Pozzi[6], A. Poglitsch[5], D. Lutz[5], R. Genzel[5], L. Tacconi[5], N. Förster Schreiber[5], E. Sturm[5], D. Elbaz[7], H. Aussel[7], E. Daddi[7], P. Andreani[8], A. Cimatti[9], R. Maiolino[10], B. Altieri[3], and I. Valtchanov[3]

[1] Instituto de Astrofísica de Canarias (IAC), 38200 La Laguna, Tenerife, Spain
e-mail: ioteo@iac.es
[2] Departamento de Astrofísica, Universidad de La Laguna (ULL), 38205 La Laguna, Tenerife, Spain
[3] Herschel Science Centre (ESAC), Villafranca del Castillo, Spain
[4] XMM/Newton Science Operations Centre (ESAC), Villafranca del Castillo, Spain
[5] Max-Planck-Institut für Extraterrestrische Physik (MPE), Postfach 1312, 85741 Garching, Germany
[6] INAF – Osservatorio Astronomico di Bologna, via Ranzani 1, 40127 Bologna, Italy
[7] Commissariat à l'Énergie Atomique (CEA-SAp), Saclay, France
[8] ESO, Karl-Schwarzchild-Str. 2, 85748 Garching, Germany
[9] Dipartimento di Astronomia, Università di Bologna, via Ranzani 1, 40127 Bologna, Italy
[10] INAF – Osservatorio Astronomico di Roma, via di Frascati 33, 00040 Monte Porzio Catone, Italy

Received 4 December 2010 / Accepted 24 January 2012

ABSTRACT

In this work we analyse the physical properties of a sample of 56 spectroscopically selected star-forming (SF) Lyα emitting galaxies at $2.0 \lesssim z \lesssim 3.5$ using both a spectral energy distribution (SED) fitting procedure from rest-frame UV to mid-IR and direct 160 μm FIR observations taken with the Photodetector Array Camera and Spectrometer (PACS) instrument onboard the *Herschel* Space Observatory. We define LAEs as those Lyα-emitting galaxies whose rest-frame Lyα equivalent widths (Lyα EW$_{\rm rest-frame}$) are above 20 Å, the typical threshold in narrow-band searches. Lyα-emitting galaxies with Lyα EW$_{\rm rest-frame}$ < 20 Å are called non-LAEs. As a result of an individual SED fit for each object, we find that the studied sample of LAEs contains galaxies with ages mostly below 100 Myr and a wide variety of dust attenuations, SFRs, and stellar masses. The heterogeneity of the physical properties is also seen in the morphology, ranging from bulge-like galaxies to highly clumpy systems. In this way, we find that LAEs at $2.0 \lesssim z \lesssim 3.5$ are very diverse, and do not have a bimodal nature, as suggested in previous studies. Furthermore, the main difference between LAEs and non-LAEs is their dust attenuation, because LAEs are not as dusty as non-LAEs. On the FIR side, four galaxies of the sample (two LAEs and two non-LAEs) have PACS detections. Their total IR luminosities place all of them in the ULIRG regime, and all are dusty objects, with $A_{1200} \gtrsim 4$ mag. This is an indication from direct FIR measurements that dust and Lyα emission are not mutually exclusive. This population of red and dusty LAEs is not seen at $z \sim 0.3$, which suggests an evolution with redshift of the IR nature of galaxies selected via their Lyα emission.

Key words. galaxies: evolution – galaxies: high-redshift – galaxies: photometry – infrared: galaxies

1. Introduction

Over the past years, a great number of galaxies have been found at different redshifts, from the local Universe up to $z \sim 7$ and even beyond. One of the most successful selection methods for searching for high-redshift galaxies is the narrow-band technique. It employs a combination of narrow- and broad-band filters to isolate the Lyα emission in the spectrum of a galaxy and to constrain its nearby continuum. This method segregates galaxies with a Lyα emission whose rest-frame Lyα equivalent width (Lyα EW$_{\rm rest-frame}$) is typically above 20 Å. They are called Lyα emitters (LAEs).

Much effort has been devoted to looking for LAEs over a wide range of redshifts (Deharveng et al. 2008; Cowie et al. 2010, 2011; Bongiovanni et al. 2010; Guaita et al. 2010; Cowie & Hu 1998; Gronwall et al. 2007; Gawiser et al. 2006; Ouchi et al. 2008; Rhoads et al. 2000; Shioya et al. 2009; Murayama et al. 2007; Ouchi et al. 2010). The physical properties of LAEs have been traditionally analysed by fitting their observed spectral energy distributions (SEDs) with Bruzual & Charlot (2003, hereafter BC03) templates. This allows the determination of their dust attenuation, star-formation rate (SFR), age, and stellar mass (Finkelstein et al. 2008, 2009a,b; Nilsson et al. 2007, 2009, 2011; Cowie et al. 2011; Ono et al. 2010; Lai et al. 2008; Pirzkal et al. 2007; Gawiser et al. 2006, 2007).

BC03 templates do not take the dust emission in the FIR into account and, even if they did, the lack of FIR information for LAEs, mainly at $z \gtrsim 2$, would cause important physical parameters, such as dust attenuation and the SFR, to have

⋆ *Herschel* is an ESA space observatory with science instruments provided by European-led Principal Investigator consortia and with important participation from NASA.
⋆⋆ Appendix A is available in electronic form at http://www.aanda.org

large uncertainties. In Oteo et al. (2011, 2012) we look for mid-IR/FIR counterparts of a sample of LAEs at $z \sim 0.3$ by using PACS-100 μm, PACS-160 μm, and MIPS-24 μm data, finding that a high percentage of them (~75%) are detected at those wavelengths. These detections enable us to determine their IR nature, dust attenuation, and SFR without the intrinsic uncertainties of SED fitting. As a result, we find that LAEs at $z \sim 0.3$ are among the least dusty galaxies at that redshift, and that the majority have total IR luminosities below 10^{11} $L_{\odot}$, i.e. are in the normal SF regime.

The $2 \lesssim z \lesssim 3.5$ range (1.7 to 3.2 Gyr after the Big Bang) is where the SFR density of the Universe has a maximum (Hogg et al. 1998; Hopkins 2004; Hopkins & Beacom 2006; Pérez-González et al. 2005; Le Floc'h et al. 2005); with respect to LAEs, this range has only started to be studied recently. Nilsson et al. (2009) demonstrate that there is significant evolution in the physical properties of LAEs between $z \sim 3.0$ and $z \sim 2.3$, with a spread in their SEDs which is wider at $z \sim 2.3$ than at $z \sim 3.0$. This indicates that LAEs at $z \sim 2.3$ are more massive, older, and/or dustier than those at higher redshifts. Nilsson et al. (2011) find that both the dust attenuation and stellar mass of LAEs at $z \sim 2.3$ are high, mainly spanning $A_V = 0.0$–2.5 mag and $\log(M_*/M_{\odot}) = 8.5$–$11.0$, respectively. They also find that physical properties of LAEs at that redshift are very diverse. Guaita et al. (2011) obtain robust determinations of mass and dust attenuation, $\log(M_*/M_{\odot}) = 8.6[8.4–9.1]$, and $E_s(B-V) = 0.22[0.00–0.31]$, for LAEs at $z \sim 2.1$. Furthermore, comparing with a sample of LAEs at $z \sim 3.1$, they find that LAEs at $z \sim 2.1$ tend to be dustier and show higher instantaneous SFR than those at $z \sim 3.1$, and that the properties are also diverse. Bond et al. (2011) claim between $z \sim 3.1$ and ~ 2.1 for an evolution of the morphological properties of LAEs, with the median half-light radii rising with decreasing redshift. They also report that LAEs at $z \sim 2.1$ are bigger for galaxies with higher stellar mass, SFR, and dust obscuration. Therefore, $2.0 \lesssim z \lesssim 3.0$ is an interesting redshift range for various reasons: 1) large samples of LAEs are being collected; 2) in this redshift range, LAEs tend to have bright observable fluxes, which allows multiwavelength coverage with a higher signal-to-noise ratio than at higher redshifts; and 3) it is a redshift range where the physical properties of LAEs seem to be changing significantly and become very diverse, whereas this has not been clearly reported at higher redshifts.

In this study, we focus on a sample of spectroscopically selected Lyα-emitting galaxies at $2 \lesssim z \lesssim 3.5$. The spectroscopic selection segregates galaxies with Lyα $\mathrm{EW}_{\mathrm{rest-frame}}$ either above or below 20 Å, the typical threshold in narrow-band searches. To place our contribution on a common base with narrow-band selected galaxies, we distinguish throughout the study between *LAEs* (Lyα-emitting galaxies with Lyα $EW_{\mathrm{rest-frame}} > 20$ Å) and *non-LAEs* (Lyα-emitting galaxies with Ly$\alpha$$\mathrm{EW}_{\mathrm{rest-frame}} < 20$ Å). The main objective of this work is to give a first glimpse at the FIR properties of LAEs at $2.0 \lesssim z \lesssim 3.5$ by using deep FIR data coming from *Herschel*-PACS observations (Poglitsch et al. 2010; Pilbratt et al. 2010). Furthermore, with the aim of better understanding this population in that redshift range, we also study their physical properties by employing a SED fitting procedure with BC03 templates. This also allows comparison between SED fitting and IR-based results.

This paper is divided in two main parts. First, in Sects. 2–5, and A.2 we describe the optical to mid-IR data used in this work, perform SED fittings with BC03 templates, and carry out a morphological analysis. Then, in Sect. 6, we focus on the FIR side of their SED, studying total IR luminosities, IR nature, total SFR, and dust attenuation for the PACS-detected galaxies. Section 7 gives the conclusions of this study.

Throughout this paper we assume a flat universe with $(\Omega_m, \Omega_\Lambda, h_0) = (0.3, 0.7, 0.7)$. All magnitudes are listed in the AB system (Oke & Gunn 1983).

2. Optical data and object selection

The sample used in this work was selected from the final data release of the VIMOS spectroscopic campaign in the GOODS-South field (Popesso et al. 2009; Balestra et al. 2010). VIMOS spectra have a quality flag assigned as follows: A (secure classification), B (likely classification) and C (tentative classification). From all the spectra in the survey, we selected only those galaxies that exhibit Lyα emission in their spectrum and which are flagged as A or B. This yields a sample of 144 objects. The wavelength coverage of the spectra implies that the LAEs are distributed within $2.0 \lesssim z \lesssim 3.5$. Throughout this article the objects are named as in Popesso et al. (2009).

With the aim of carrying out SED fits for the galaxies studied, we used the MUSIC multi-wavelength photometric catalogue (from 0.3 to 24.0 μm) of a large and deep area in the GOODS-South Field. Its first version was made by Grazian et al. (2006), and a subsequent update was elaborated by Santini et al. (2009). The former uses F435W, F606W, F775W, and F850LP ACS images, JHK_s ISAAC data, mid-IR data provided by IRAC instrument (3.6, 4.5, 5.8, and 8.0 μm), and publicly available U-band data from WFI and VIMOS. The z-band of ACS GOODS frames and K_s of VLT images were used to select objects in the field, yielding a unique, self-consistent catalog. The details of the catalogs (object detections, PSF-matchings, limiting magnitudes, etc.) can be found in Grazian et al. (2006). The second version includes objects selected from the IRAC-4.5 μm image and therefore sources detected at that wavelength but very faint or undetected in the K_s band. MIPS-24 μm photometry is also included although it will not be considered in the SED fittings (see Sect. 3). Owing to these improvements, we adopted the second version of the photometric catalog.

To build our final sample of Lyα-emitting galaxies, we matched the coordinates of 144 spectra with the MUSIC catalogue, resulting in a total of 70 objects. The area covered by the VIMOS spectroscopic observations is larger than the GOODS-MUSIC footprint, and this results in the loss of 50% of the sources. From this common sample, we visually inspected each spectrum, ruling out objects with no clear Lyα emission or with AGN ionization lines present in their spectra. We finally obtained a clean sample of 56 Lyα-emitting galaxies whose optical spectra suggest that they have a star-forming (SF) nature. Figure 1 shows the redshift distribution of the objects in the final sample. It can be seen that most of them are at $2.0 \lesssim z \lesssim 2.7$, although we also have a significant number of sources at $z \gtrsim 3$. Figure 2 shows the distribution of the observed V-band magnitude of the galaxies studied. Most of them are brighter than 25.5 mag in that band, which is comparable to the brightness of the UV-bright subsample defined in Guaita et al. (2011). The main advantage of working with a continuum-bright sample is that it is possible to carry out individual SED fitting for each galaxy, avoiding the uncertainties of stacking (Nilsson et al. 2011).

3. SED fitting method

We performed SED fittings with BC03 templates for the sample of 56 galaxies by using the Zurich Extragalactic Bayesian

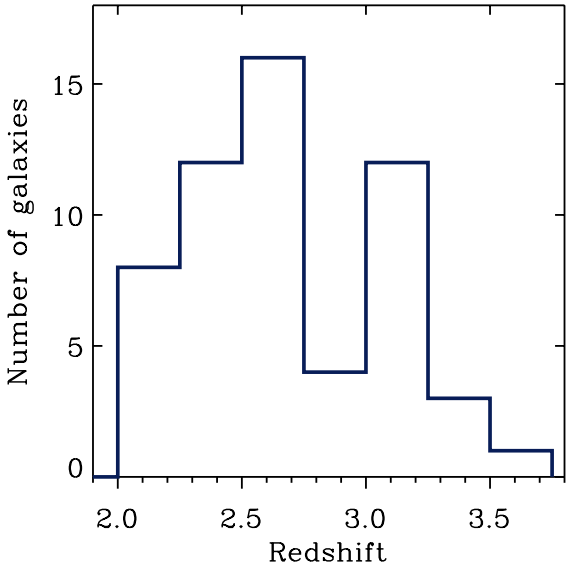

Fig. 1. Redshift distribution of the sources in the final sample. We study objects at $2 \lesssim z \lesssim 3.5$.

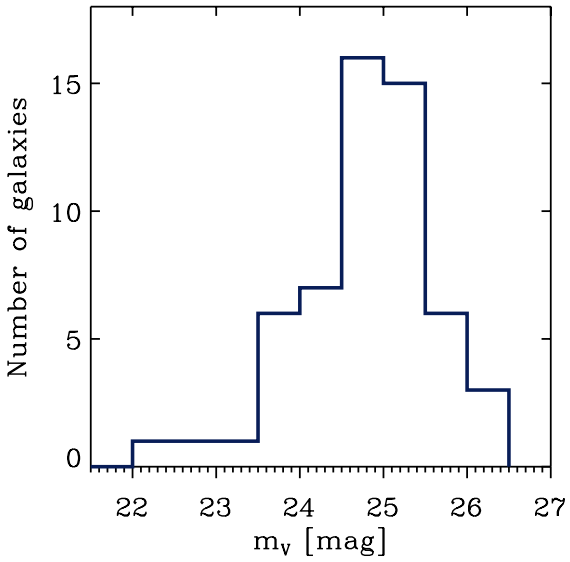

Fig. 2. Histogram of the magnitudes in the V band of the final sample of 56 LAEs. The values appearing here are similar to those in the UV-bright sample of Guaita et al. (2011).

Redshift Analyzer (ZEBRA, Feldmann et al. 2006). In its maximum-likelihood mode, ZEBRA employs a χ^2 minimization algorithm over the templates to find the one that fits the observed SED of each object best. In this process, we excluded the MIPS-24 μm measurements, since the fluxes in this band have a significant contribution of warm dust and PAH molecule emission, which are not taken into account in the BC03 templates. We employed `GALAXEV`, which is provided by BC03, to build a large sample of templates. In this process we adopted a Salpeter (1955) initial mass function (IMF), distributing stars from 0.1 to 100 $M_\odot$. This IMF has mostly been used in previous works in the studied redshift range (Guaita et al. 2011; Nilsson et al. 2011; Lai et al. 2008; Ono et al. 2010; Gawiser et al. 2006, 2007). Since metallicities do not significantly modify the shape of the SEDs of galaxies, we adopted $Z = 0.4\ Z_\odot$. Different authors employ different values: Lai et al. (2008) and Guaita et al. (2011) consider the solar metallicity, whereas Ono et al. (2010) utilize a value of 0.2 $Z_\odot$. To check the validity of our choice, we ran ZEBRA with BC03 templates associated with different metallicities and we find similar results for the other parameters, within the uncertainties. This, at the same time, is an indication that metallicity is difficult to determine accurately with SED fitting. For the SFR, we used models with temporally constant values, as in many previous studies (Gawiser et al. 2006; Lai et al. 2008; Ono et al. 2010; Guaita et al. 2011; Kornei et al. 2010). In this case, the SFR can be obtained from the rest-frame UV fluxes once the templates are normalized to fit the observed photometry and employing the Kennicutt (1998) calibrations. We also tried to use exponentially decreasing SFRs, but the differences between the results for age and dust attenuation were not significant. Ono et al. (2010) also compare the results obtained with constant and varying SFRs and find similar results in both cases, which indicates that the history of the star formation in a galaxy is hard to constrain with SED-fitting methods. Furthermore, adopting an exponentially varying SFR would add a new degree of freedom in the process, the star formation time scale, introducing more uncertainties in the determination of the other parameters.

The ages considered here span from 1 Myr to 3.4 Gyr, the age of the Universe at the minimum redshift of the sample, $z \sim 2.0$. Dust attenuation is included via the Calzetti et al. (2000) law with values of the colour excess in the stellar continuum, $E_s(B-V)$, ranging from 0 to 0.7 in steps of 0.05. We also include intergalactic medium absorption adopting the prescription of Madau (1995). Stellar masses are obtained from SFR and age, according to the assumed temporal variation of the SFR. Regarding the uncertainties in the fitted values, ZEBRA provides a parameter related to the probability that one template truly represents the observed photometry of a given source. In the SED fitting of each galaxy, we select all the templates whose associated probability is above 68% and consider the uncertainty of each parameter as the average of the values associated with that parameter on those selected templates.

4. Stellar populations

Figure 3 and Table A.1 show the results of the SED fitting for the studied galaxies. The dust attenuation of the studied LAEs, parameterized by the colour excess in the stellar continuum $E_s(B-V)$, ranges from 0 to 0.3, with a median value of 0.15. The uncertainties in dust attenuation have a lower limit equal to the sampling of this parameter in the templates, that is, $\Delta E_s(B-V) \sim 0.05$, and are also affected by the well-known degeneracy between age, dust attenuation, and metallicity of the SED-fitting methods. Despite the uncertainties, the values obtained here are distributed within approximately the same interval as that in Guaita et al. (2011) for the UV-bright sample, although their median value, $E_s(B-V) \sim 0.32$, is higher than that found in the present study.

Regarding age, the studied LAEs are young galaxies, most of them having ages below 100 Myr. However, there are some LAEs (~20%) whose SEDs are compatible with older populations, above 300 Myr. Although the threshold age in the generation of the templates was set to the age of the Universe at $z \sim 2$, there is no violation of the age of the universe for galaxies at higher redshifts. The uncertainties in age are typically below 20%, which hints at robust age estimates.

Intense rest-frame optical emission lines, such as [OII], [OIII] and Hα, could have a strong effect on the observed broadband photometry of a galaxy. At $z \sim 0.3$, Cowie et al. (2011) employed their rest-frame optical spectroscopic observations of their LAEs to analyse the influence of rest-frame

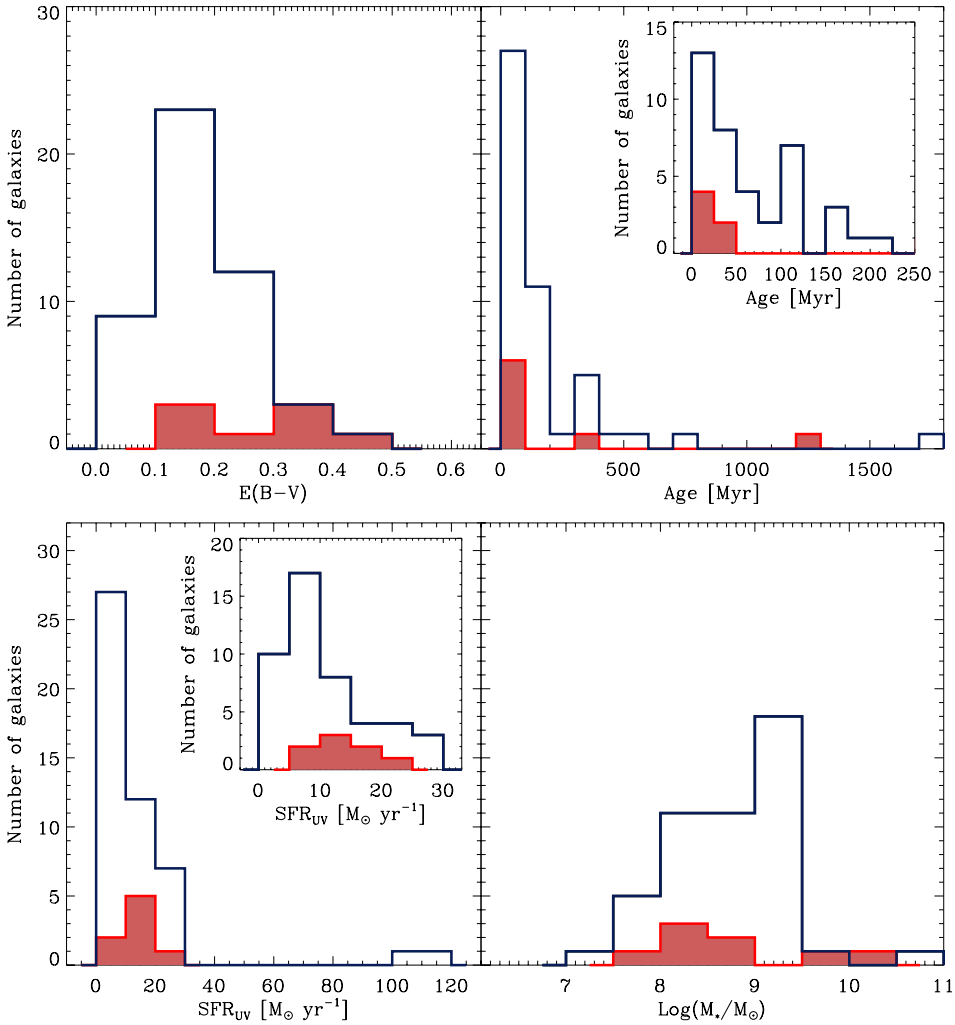

Fig. 3. Distribution of the physical properties for the sample of 56 LAEs. Blue- and red-shaded histograms represent LAEs and non-LAEs, respectively. Inset plots are more detailed representations of the zones of the histograms where most objects are located.

optical emission lines on the derived parameters in a SED-fitting procedure. As a result, it was found that not subtracting those lines overestimates the ages of the LAEs in their sample. In our study, given that we do not have spectral information about the [OII], [OIII], or Hα emission for the galaxies studied, we cannot correct for this effect, so the ages obtained here should be considered as an upper limit of the real values.

Since the LAEs studied have a bright UV continuum, their dust-uncorrected SFRs (SFR$_{\rm UV,uncorrected}$) are high, ranging from about 2 to 100 $M_\odot\,{\rm yr}^{-1}$, with a median of SFR$_{\rm UV,uncorrected}$ $\sim$ 10 $M_\odot\,{\rm yr}^{-1}$. These values are slightly higher than those reported at lower redshifts. In Oteo et al. (2012) we studied the SFR$_{\rm UV,uncorrected}$ for LAEs at $z \sim 0.3$, finding that most of them have SFR$_{\rm UV,uncorrected}$ below 5 $M_\odot\,{\rm yr}^{-1}$. We see no such low values because of the UV-brightness of the LAEs studied. However, the high values found at $2.0 \lesssim z \lesssim 3.5$ are not seen at $z \sim 0.3$. This could suggest that the upper limit of the SFR$_{\rm UV,uncorrected}$ in LAEs is increasing from 0.3 to $z \gtrsim 2$, or similarly, that there is an evolution in the upper limit of the UV luminosity, $L_{\rm UV}$. The surveyed comoving volume in Oteo et al. (2012) and in this study are similar, given that the GALEX observations used in the former cover a much larger area of the sky than those used here: the much larger surveyed area at $z \sim 0.3$ makes up for the difference in redshifts. Cowie et al. (2011) report strong evolution in the Lyα luminosity function of LAEs between $z \sim 0.3$ and ~1.0, which could be related to the evolution in the upper limit of $L_{\rm UV}$ reported above. This suggests that there is a noticeable change in the UV properties of galaxies selected via their Lyα emission from $z \sim 0.3$ to $z \gtrsim 2.0$.

The stellar mass of our LAEs lies within the range $7.0 \lesssim \log(M_*/M_\odot) \lesssim 9.5$. More than 70% of the Lyα-emitting galaxies studied are detected in IRAC-3.6 μm under a similar limiting luminosity as that in Lai et al. (2008). In this way, we are working with a sample of IRAC-bright sources, and they should be among the most massive LAEs in the redshift range studied. The range of stellar masses obtained here is compatible with the results of Guaita et al. (2011) for the UV-bright sample and with those at $z \sim 3.0$ of Lai et al. (2008) and Gawiser et al. (2006, 2007) for both IRAC-detected and IRAC-undetected stacked samples.

After inspecting the individual SED fits shown in Fig. A.1, it can be seen that there is a wide range of shapes, from almost dust-free cases with a negative UV continuum slope to highly attenuated LAEs with a positive UV continuum slope. The rest-frame optical-to-UV colours also show a significant variation from blue to red objects. This way, analysing individual SEDs for each object, we find LAEs with very different properties, rather than the double nature suggested in previous works, which could be the result of the stacking method employed (Lai et al. 2008; Gawiser et al. 2006, 2007). Actually, Nilsson et al. (2011) studied the effects of stacking in their sample of LAEs at $z \sim 2.3$ and found that, while stellar masses are robust to stacking, ages and dust attenuation tend to be incorrectly determined. Therefore, it is clear that to analyze the

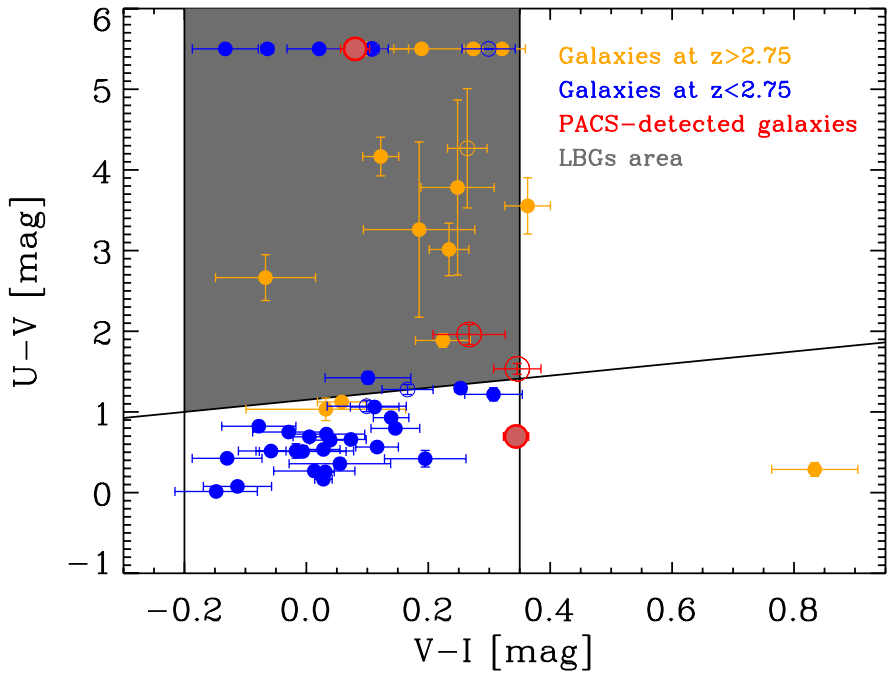

Fig. 4. Colour–colour diagram containing the locus of LBGs according to Pentericci et al. (2010). Filled and open dots represent LAEs and non-LAEs, respectively. Orange and blue dots represent galaxies at $z > 2.75$ and $z < 2.75$, respectively. Red dots are PACS-detected galaxies and shaded zone is the area where LBGs are located. For clarity, the galaxies with a $U - V$ colour greater than 5.5 are assigned $U - V = 5.5$.

physical properties of LAEs at high redshift, individual fits to the observed photometry are needed, although it is challenging for those LAEs at $z \gtrsim 3$ owing to photometric limitations. Actually, only a few LAEs of the samples of Ono et al. (2010) and Lai et al. (2008) are detected in the K_s band, which, at their redshifts, is quite important for sampling the Balmer break and obtaining accurate values of age, and stellar mass. Results based on stacking analysis must be treated with care, most importantly in those cases where the SEDs are known to have very diverse shapes and properties, as shown in this and previous studies to occur at $2.0 \lesssim z \lesssim 3.5$ (Guaita et al. 2011; Nilsson et al. 2011).

As mentioned in Sect. 1, the spectroscopic selection used in this study allows us to isolate sources with Lyα $EW_{\rm rest-frame} < 20$ Å (non-LAEs). However, the number of such sources in our sample is low. Non-LAEs are also represented in Fig. 3. It can be seen that the age, SFR and mass of these galaxies are in the same range as those for LAEs. The main difference is the dust attenuation: objects with an attenuated Lyα emission are among the dustiest objects in the sample. This points towards the idea that LAEs are among the least dusty galaxies at each redshift, as reported in other studies at different redshifts (Cowie et al. 2011; Oteo et al. 2011, 2012; Pentericci et al. 2007, 2010; Kornei et al. 2010).

Figure 4 represents the locus of Lyman-break galaxies (LBGs) at $z \sim 3.0$ for the filters in the MUSIC survey (Pentericci et al. 2010). It can be seen that some LAEs could also have been selected as LBGs. The subsample of LAEs with colours of LBGs (LAE-LBGs) is the bridge population between these two kinds of galaxies. The principal difference between LAE-LBGs and the total sample of LAEs is the dust attenuation: LAE-LBGs tend to be dustier than other LAEs. In Fig. 4, this tendency is reflected in their $V - I$ colour. At our redshifts, this colour measures the UV continuum slope, and higher values correspond to greater dust attenuation. Being dustier, LAE-LBGs have higher $V - I$ colour (redder UV continuum) than other LAEs in the sample. Pentericci et al. (2010) find that LBGs with Lyα emission at our redshift have lower dust attenuation than those without Lyα line. The combination of both results points towards a sequence of increasing dust attenuation, from the less-dusty non-LBG LAEs, to dustier LAE-LBGs and finally those LBGs without Lyα emission, so they could be the same population differentiated by dust attenuation.

5. Morphology

By using HST/ACS images in GOODS-South we carried out a morphological analysis of the 56 Lyα-emitting galaxies. We adopted the classification given in Elmegreen et al. (2009) and visually classified them into three groups: 37 clump clusters (CC), 8 chain galaxies (CH), and 11 spiral-bulges (SPB). This classification was done by three different people and the results were similar. Most LAEs in our sample have irregular morphologies (CH or CC), indicating processes of ongoing formation. Figure A.2 shows the ACS optical cut-outs of the 56 LAEs of our sample in the ACS B, V, I, and Z photometric bands. It can be seen that there is a wide variety of sizes and morphologies, from highly compact to highly clumpy objects. This heterogeneity in morphology is compatible with the wide range of physical properties for our LAEs reported in the previous section, indicating that galaxies segregated by their Lyα emission at our redshift do not have specific properties, but instead can be very diverse.

We fitted the SPB LAEs, which are all at $z < 2.75$, with Sersic (1968) profiles by using `GALFIT` (Peng et al. 2010) in the z-band images. At our redshift, this band represents the emission of the rest-frame optical light near the Balmer break. The Sersic profiles can be analytically described by

$$I(r) = I_b(0) \exp\left[-b_n \, (r/R_{\rm eff})^{1/n}\right] \quad (1)$$

where $I_b(0)$ is the central intensity, $R_{\rm eff}$ the effective radius, and n the Sersic index. Figure 5 shows how GALFIT performs the fits in three randomly selected SPB LAEs, which are representative of the behaviour of the total sample of SPB LAEs. It can be seen that the Sersic (1968) profiles describe the morphology of these objects quite well. To obtain the intrinsic $R_{\rm eff}$ in kpc from

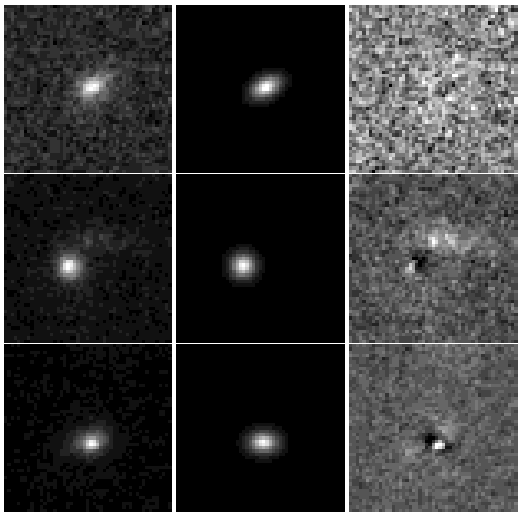

Fig. 5. Examples of GALFIT fittings for three SPB LAEs. *Left*: images of the LAEs. *Middle*: Sersic fitted profiles. *Right*: residuals of the fittings.

the output value given by GALFIT (in pixels), we made use of the assumed cosmology and the ACS pixel scale. As the result, we find that the SPB LAEs have effective radii ranging from 2.6 to 3.1 kpc. The uncertainty in the effective radius, which is provided by GALFIT, is less than 5%. This range is compatible with the tail of the distribution at large effective radii found in Bond et al. (2009) at $z \sim 3.1$, in Bond et al. (2011) at $z \sim 2.1$, and in Oteo et al. (2012) at $z \sim 0.3$. Therefore, no evolution of the physical sizes of LAEs with redshift is seen with the present data.

Regarding the Lyα EW$_{\rm rest-frame}$, we do not find any significant difference in the morphology of LAEs and non-LAEs, because of the scarcity of galaxies in the non-LAE sample. Pentericci et al. (2010) show that at our redshift, the rest-frame UV morphology does not depend strongly on the presence of the Lyα emission. At $z \sim 0.3$, in Oteo et al. (2012) we find that LAEs and non-LAEs show a clear difference in their morphology, both in shape and size, which indicates that at that redshift Lyα photons are escaping from small and irregular/merging galaxies.

6. *Herschel* FIR counterparts

GOODS-South was observed with PACS-70 μm, PACS-100 μm, and PACS-160 μm in the frame of the PACS evolutionary probe project (PEP, PI D. Lutz). PEP is the *Herschel* guaranteed time key-project designed to obtain the best profit from *Herschel* instrumentation to study the FIR galaxy population (Lutz et al. 2011). PACS fluxes used in this work were extracted using MIPS-24μm position priors with, at least, a 3σ significance. Limiting fluxes in PACS-70 μm, PACS-100 μm, and PACS-160 μm are 1.0 mJy, 1.1 mJy, and 2.0 mJy, respectively. We look for possible FIR counterparts of our galaxies within 2″, which is the typical astrometric uncertainty in the position of the sources, finding four detections in at least the PACS-160 μm band. PACS-detected sources are GOODS_LRb_001_q2_9_1, GOODS_LRb_001_q3_9_1, GOODS_LRb_001_q1_8_1, and GOODS_LRb_dec06_3_q3_60_1. These counterparts are direct evidence of dust emission in high-redshift SF sources. As seen in Fig. A.2, GOODS_LRb_001_q2_9_1, GOODS_LRb_001_q3_9_1 and GOODS_LRb_001_q1_8_1 are isolated sources; therefore, the dust emission comes entirely from these sources. However, GOODS_LRb_dec06_3_q3_60_1 has a nearby galaxy whose emission in the FIR could contaminate the FIR flux of this galaxy. Two of the PACS-detected galaxies are within the LAE group (GOODS_LRb_001_q2_9_1 and GOODS_LRb_001_q1_8_1) and the other two (GOODS_LRb_001_q3_9_1 and GOODS_LRb_dec06_3_q3_60_1) have Lyα EW$_{\rm rest-frame}$ compatible with their being non-LAEs. Figure 6 represents the rest-frame UV to FIR SED of the four PACS-detected galaxies.

Table 1 shows the dust attenuation and SFR$_{\rm UV,uncorrected}$ of the four PACS-detected galaxies, as derived from SED fitting. Their rest-frame UV to mid-IR SEDs are compatible with high values of dust attenuation, and the two LAEs also exhibit greater SFR$_{\rm UV,uncorrected}$ than the median value of the sample. Their large SFR$_{\rm UV,uncorrected}$ indicates that they have high UV luminosity, compatible with the greater likelihood that UV-bright galaxies are detected in the FIR (Reddy et al. 2010). GOODS_LRb_001_q2_9_1, GOODS_LRb_001_q3_9_1 and GOODS_LRb_dec06_3_q3_60_1 are young objects with masses similar to the median population. However, GOODS_LRb_001_q1_8_1 is an old and dusty LAE and is among the most massive objects of the sample. This is one of the most interesting galaxies in our sample, since its physical properties are opposite to the classical idea of LAE, i.e. a young, less massive, and dust-free galaxy. Three out of the four PACS-detected galaxies would have been selected via the Lyman break technique (see Fig. 4). It can be seen that PACS-detected sources have among the highest $V - I$ coloors of the total sample, indicating that they have a highly attenuated UV continuum, compatible with their being among the dustiest galaxies in our sample.

6.1. IR luminosities

Accurate values of the total 8–1000 μm IR luminosities, $L_{\rm IR}$, can be obtained for the PACS-detected galaxies. Since we do not have full coverage of the dust emission peak, we cannot calculate $L_{\rm IR}$ by direct integration of the FIR SED. Instead, we convert PACS fluxes into $L_{\rm IR}$ by using Chary & Elbaz (2001) (hereafter CE01) templates, which have only one solution for $L_{\rm IR}$ for each FIR flux and redshift. Obtaining $L_{\rm IR}$ by using single FIR band extrapolations has been employed with success in previous studies of galaxies at similar redshifts (Nordon et al. 2010; Elbaz et al. 2010, 2011). In fact, by combining PACS and SPIRE measurements, Elbaz et al. (2010) show that fitting CE01 templates to the PACS-160 μm flux provides reliable estimates of $L_{\rm IR}$ at our redshift. The typical uncertainties in the derived values are related to the accuracy of singl-band extrapolations rather than to uncertainties in the PACS fluxes themselves, and are typically less than 0.2 dex (Elbaz et al. 2011). Actually, for galaxies in our redshift range, PACS-160 μm band extrapolations give the most accurate results for single band extrapolations (Elbaz et al. 2010).

6.2. LAE–ULIRGs relation

Previous results suggest that some LAEs in our redshift range are also ultraluminous infrared galaxies (ULIRGs) (Nilsson & Møller 2009; Nilsson et al. 2011; Ono et al. 2010; Chapman et al. 2005), but direct detections in the FIR around the dust emission peak have not yet been reported. In this study, according to their $L_{\rm IR}$, the four PACS-detected galaxies have a ULIRG nature. Owing to the depth of the PACS observations used in this study, the limiting $L_{\rm IR}$ is about $10^{12}\,L_{\odot}$ at $z \sim 2.2$. Therefore, there could be some PACS-undetected LAEs in our sample, the dustiest at the highest redshifts, that fall in the ULIRG class.

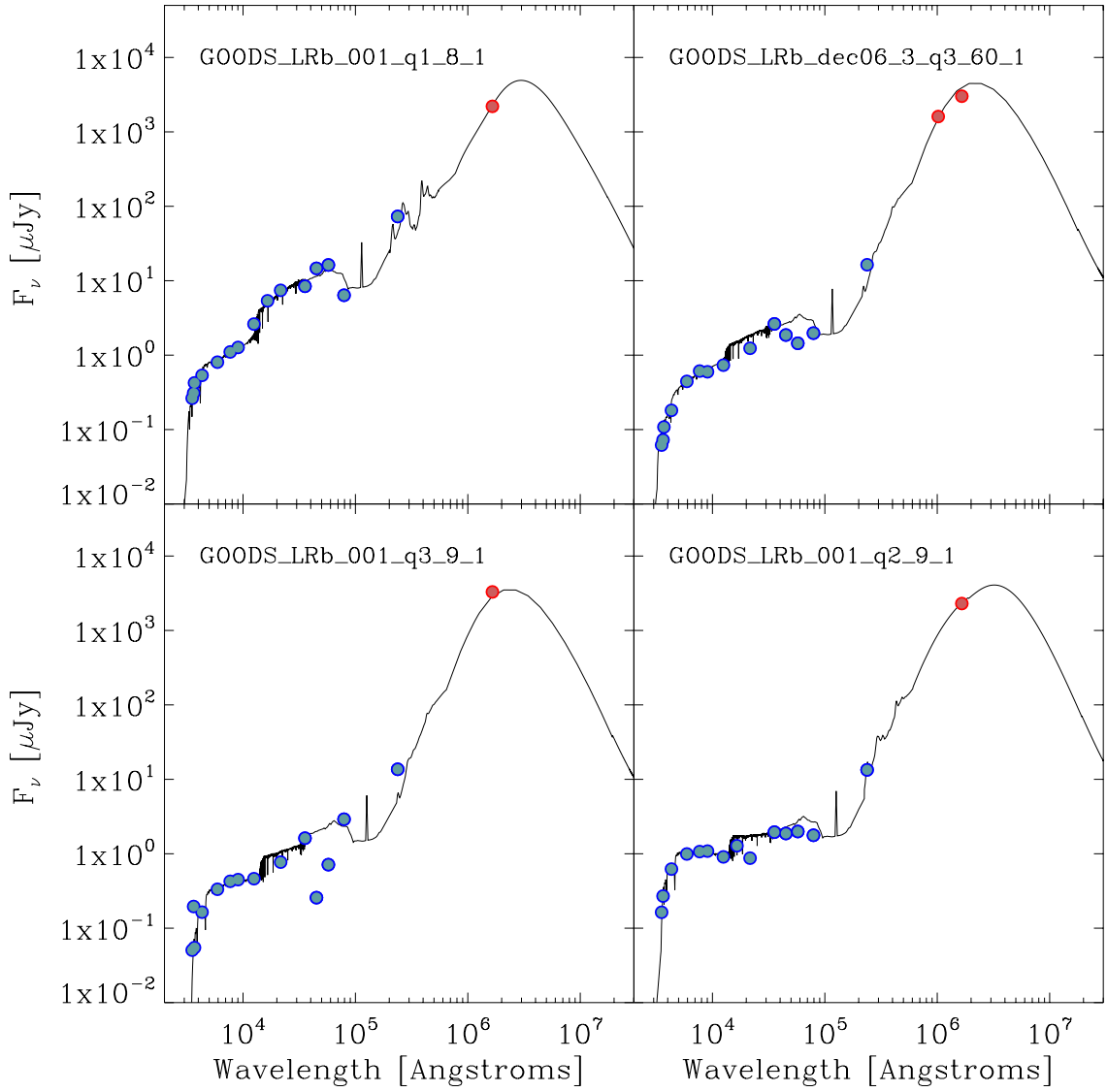

Fig. 6. Optical-to-FIR observed SED of the PACS-detected Lymanα emitting galaxies. Blue dots represent the multi-wavelength photometry from U-band to MIPS-24 μm, and red dots are the PACS-100 μm and/or PACS-160 μm fluxes. The black curve represents the combination of BC03 and CE01 templates that best fit the photometric data for each galaxy.

Actually, given that FIR detections segregate dusty galaxies, it is expected that the dustiest LAEs, $E_s(B-V) \gtrsim 0.2$ of the sample have a ULIRG nature even when PACS-undetected. The number of LAEs with a ULIRG nature found, although low, is of great importance. In Oteo et al. (2011, 2012) we studied the FIR properties of a sample of 23 mid-IR/FIR detected LAEs at $z \sim 0.3$ and found that most LAEs are in the normal SF galaxy regime, $L_{\rm IR} < 10^{11}\,L_\odot$, with only one having $L_{\rm IR} \sim 10^{11.5}\,L_\odot$, and none above that value. The discovery of LAEs with a ULIRG nature at $z \sim 2.4$–2.8 suggests that the IR properties of LAEs evolve from $z \sim 0.3$ to $\sim$2.5 in the sense that there is a population of red and dusty LAEs that is not seen at lower redshifts. Therefore, from direct FIR detections, we find that the ULIRG fraction in LAEs decreases from $z \sim 2.4$–2.8 to $\sim$0.3, following the trend found for IR-detected galaxies between those redshifts (see for example Le Floc'h et al. 2005).

This possible evolution of the IR emission, along with the reported evolution in the UV luminosity (Sect. 4) and in the Lyα luminosity function from $z \sim 1.0$ (Cowie et al. 2011), indicates that either the Lyα selection technique does not trace the same kind of objects with redshift, or the properties of Lyα-selected galaxies change with redshift.

6.3. Dust attenuation

The ratio between IR and UV luminosities is the best way to obtain the dust attenuation in galaxies. Adopting the Buat et al. (2005) calibration, the dust attenuation for our PACS-detected Lyα-emitting galaxies can be obtained with the expression

$$A_{\rm NUV} = -0.0495x^3 + 0.4718x^2 + 0.8998x + 0.2269 \quad (2)$$

where, $x = \log(L_{\rm IR}/L_{\rm NUV})$. The conversion from dust attenuation in the NUV band into the colour excess in the stellar continuum is carried out by using the Calzetti et al. (2000)

Table 1. Dust attenuation as derived from SED fitting, $E_s(B-V)$ [BC03], and from the IR/UV ratio, $E_s(B-V)$ [IR/UV], dust-uncorrected SFR, $SFR_{UV,uncorr}$, dust-corrected SFR, $SFR_{dust-corr}$, and total SFR, SFR_{total}, for the four PACS-detected sources.

Object	$E_s(B-V)$ [BC03]	$E_s(B-V)$ [IR/UV]	$SFR_{UV,uncorr}$ [$M_\odot\,yr^{-1}$]	$SFR_{dust-corr}$ [$M_\odot\,yr^{-1}$]	SFR_{total} [$M_\odot\,yr^{-1}$]
GOODS_LRb_001_q1_8_1	0.20	0.40	19.6	74.9	242.3
GOODS_LRb_dec06_3_q3_60_1	0.40	0.48	11.9	172.7	311.2
GOODS_LRb_001_q3_9_1	0.30	0.57	10.7	80.1	452.8
GOODS_LRb_001_q2_9_1	0.15	0.42	25.6	70.3	341.5

reddening law. The values obtained are shown in Table 1 and all are $E_s(B-V) \gtrsim 0.4$. PACS-detected LAEs have high values of dust attenuation and since they are selected via their IR emission, those values represent an upper limit of the dust attenuation of LAEs in the redshift range studied. This is a direct indication from FIR measurements that the Lyα emission and the presence of dust are not mutually exclusive. This result could reinforce the scenario in which the Lyα emission can be enhanced under a suitable geometry (Neufeld 1991), for which evidence has already been found at higher redshifts (Finkelstein et al. 2008), but not at our redshift or lower (Guaita et al. 2011; Finkelstein et al. 2011; Blanc et al. 2011). The dust attenuation derived from SED fitting tends to be lower than that obtained from direct IR/UV measurements. The ULIRG nature plays an important role in this underestimation, since in this case the IR emission is more prominent than in other less IR-luminous galaxies and its inclusion in the analysis is essential for obtaining accurate results.

6.4. SFR

The combination of UV and IR luminosities provides the best determination of the SFR in galaxies. Assuming that all the light absorbed in the UV is in turn reradiated in the FIR, the total SFR of a galaxy, SFR_{total}, can be obtained as the sum of $SFR_{UV,uncorrected}$ plus a correction term associated with the dust emission in the FIR. Adopting the Kennicutt (1998) calibration, that correction term can be written as

$$SFR_{IR}[M_\odot\,yr^{-1}] = 4.5\times10^{-44} L_{IR}\,[erg\,s^{-1}] \quad (3)$$

where L_{IR} is defined in the same way as in Sect. 6.1. In this way, SFR_{total} can be inferred from:

$$SFR_{total} = SFR_{UV,uncorrected} + SFR_{IR}. \quad (4)$$

The values of SFR_{total} obtained for the PACS-detected galaxies are also shown in Table 1. Such sources have high SFR_{total} all above 200 $M_\odot\,yr^{-1}$. PACS-deteced sources are the reddest ones in the sample and the fastest star formers. Although the number of such kind of galaxies is low, their SFRs can be considered as the maximum value of the SFRs for LAEs in the redshift range studied. It can be also seen that the contribution of the SFR_{IR} to the SFR_{total} is quite high, above 93% in all cases; therefore, SED fitting with BC03 templates, which do not take the dust emission in the FIR into account, systematically underestimates this quantity. Since we do not have a statistically significant sample of LAEs detected in the FIR, we cannot evaluate a typical factor of underestimation for LAEs in our redshift range. In Oteo et al. (2012) we found that, for LAEs at $z \sim 0.3$, the contribution of the FIR emission is more than 60% in most cases so that an SFR based on SED fitting is underestimate by a factor greater than 2. According to the IR evolution reported in Sect. 6.2, it might be expected that the FIR contribution could be higher than 60% for a high percentage of the sample. Actually, LAEs at $z \sim 2.0$ with $L_{IR} \gtrsim 10^{10.5}\,L_\odot$ are unlikely to be detected with the current FIR surveys, and their IR contribution to the SFR_{total}, assuming an $SFR_{UV,uncorrected} \sim 10\,M_\odot\,yr^{-1}$, is about 50%.

By using the dust attenuation derived from SED fitting, we could correct the $SFR_{UV,uncorrected}$ to estimate the SFR_{total}. Their values are also shown in Table 1. It can be seen that the SFR_{total} obtained in such a way are much lower than the values obtained from the combination of IR/UV emissions. This agrees with Wuyts et al. (2011), who report that SED fitting tend to underestimate the total amount of star formation in IR-bright galaxies at $z \gtrsim 2.5$.

Table 2. Total infrared luminosities for the MIPS-24 μm detected LAEs.

Object	Redshift	$Log(L_{IR}/L_\odot)$
GOODS_LRb_002_1_q3_8_1	2.296	12.34
GOODS_LRb_002_1_q2_60_1	2.181	11.30
GOODS_LRb_dec06_2_q2_12_1	2.318	12.10
GOODS_LRb_dec06_3_q1_21_1	2.230	11.97
GOODS_LRb_002_1_q4_66_1	2.586	12.29
GOODS_LRb_dec06_3_q4_53_1	2.702	11.62

Notes. PACS-detected LAEs, which are also detected in MIPS-24 μm are not included in this table.

6.5. MIPS-24 μm counterparts of LAEs

In addition to the analysed measurements in PACS-160 μm, six other PACS-undetected galaxies of the total sample of 144 have MIPS-24 μm detections in the FIR regime, which were found following the same criterion as that used for PACS counterparts. All these galaxies are classified as LAEs. None of them is within the MUSIC footprint; we cannot therefore analyse the distinctive properties of MIPS-24 μm-detected LAEs regarding the rest-frame UV to mid-IR SED fitting. The MIPS-24 μm detections also indicate the presence of IR-bright, i.e. dusty, LAEs. At $2.0 \lesssim z \lesssim 3.5$, the MIPS-24 μm band has a significant contribution of PAH molecule emission, which prevents us from determining the L_{IR} for MIPS-detected LAEs. Actually, Elbaz et al. (2010) study the validity of MIPS-24 μm extrapolations to the L_{IR} and find that they are valid up to $z \sim 1.5$ and for objects that are below the ULIRG limit. At $z \gtrsim 1.5$, MIPS-24 μm extrapolations tend to overestimate the L_{IR} by a factor of about 2–3. Despite this overestimation, we show the L_{IR} luminosities for the MIPS-24 μm-detected LAEs in Table 2 as inferred from MIPS-24 μm single-band extrapolation, as in Sect. 6.1 for PACS-detected sources. Owing to the PACS catalogues used in Sect. 6, PACS-detected LAEs are also detected in MIPS-24 μm but we do not consider those objects here because they have been more

accurately studied in previous sections. It can be seen in Table 2 that, although overestimated, MIPS-24 μm-detected LAEs have high values of L_{IR}, placing them at least in the LIRG regime, $L_{\rm IR} > 10^{11}\,L_{\odot}$. Therefore, in total we gather a sample of ten red and dusty LAEs, which are opposite to the classical idea of LAEs as dust-free galaxies.

7. Summary and conclusions

In this work we have analysed the rest-frame UV to IR SED of a sample of 56 Lyα-emitting galaxies at $2.0 \lesssim z \lesssim 3.5$. According to their Ly$\alpha$ EW$_{\rm rest-frame}$ we distinguish between LAEs and non-LAEs as those Lyα-emitting galaxies with Lyα EW$_{\rm rest-frame}$ above and below 20 Å, respectively. This value is the typical threshold in narrow-band searches. Our main conclusions are as follows.

1. Individual SED fits for our LAEs indicate that they are mostly young galaxies with ages below 100 Myr, although some of them have SEDs compatible with populations older than 300 Myr. The dust attenuation ranges from low, $E_{\rm s}(B-V) \sim 0.0$, to high values, $E_{\rm s}(B-V) \sim 0.3$, with a median of $E_{\rm s}(B-V)$ of 0.15. The SFRs, as derived from UV dust-uncorrected measurements, range from about 2 to 100 $M_{\odot}$ yr^{-1}, mostly having $SFR_{\rm UV,uncorrected} \sim 10\,M_{\odot}$ yr^{-1}.
2. We find that LAEs at $2.0 \lesssim z \lesssim 3.5$ show a wide range of properties, rather than having a double nature, as suggested in previous studies. It has been possible to achieve this result because our LAEs are continuum-bright objects; therefore, we were able to carry out an individual SED fit for each source.
3. The variety of the physical properties of LAEs is also reflected in their morphology. We find many different structures, from bulge-like galaxies to highly clumpy systems or chain galaxies. Fitting the bulge-like LAEs to Sersic profiles, we found sizes distributed within 2.6 and 3.1 kpc, compatible with those reported in other studies at higher, similar, and lower redshifts.
4. We find four Lyα-emitting galaxies with PACS-FIR counterparts, two LAEs, and two non-LAEs. This indicates that some LAEs have such a high dust content that its emission can be directly detected. Their rest-frame UV to mid-IR SEDs are compatible with objects with high dust attenuation. FIR-detected LAEs are objects with high SFR, above 200 $M_{\odot}$ yr^{-1}, and their $L_{\rm IR}$ classify them as ULIRGs. LAEs with an ULIRG nature are not seen at $z \sim 0.3$, suggesting that there is evolution in their IR emission with redshift. This, along with the rapid evolution of the Lyα luminosity function from $z \sim 0.3$ to $\sim$1.0 reported in previous studies and the evolution in the $L_{\rm UV}$ from $z \sim 0.3$ to $z \gtrsim 2.0$ found here, indicates that either the physical properties in the UV, optical, and IR of objects that are selected via their Lyα emission change with redshift, or the Lyα selection technique segregates different types of galaxies at different redshifts.
5. We obtained the dust attenuation for the PACS-detected LAEs with MUSIC counterparts by combining UV and FIR information, without the uncertainties of the SED-fitting based methods. The results obtained in this way show that they have colour excesses greater than 0.30 in their stellar continuum. This indicates that PACS-detected LAEs are dusty objects, despite having a Lyα line emission in their spectra. This confirms from direct FIR observations that dust and Lyα emission are not mutually exclusive.

Acknowledgements. This work was supported by the Spanish Plan Nacional de Astrononomía y Astrofísica under grant AYA2008-06311-C02-01 and is based on observations made with ESO Telescopes at the La Silla or Paranal Observatories under programme ID 171.A-3045. PACS has been developed by a consortium of institutes led by MPE (Germany) and including UVIE (Austria); KUL, CSL, IMEC (Belgium); CEA, OAMP (France); MPIA (Germany); IFSI, OAP/AOT, OAA/CAISMI, LENS, SISSA (Italy); IAC (Spain). This development has been supported by the funding agencies BMVIT (Austria), ESA-PRODEX (Belgium), CEA/CNES (France), DLR (Germany), ASI (Italy) and CICYT/MICINN (Spain). The Herschel spacecraft was designed, built, tested, and launched under a contract to ESA managed by the *Herschel/Planck* Project team by an industrial consortium under the overall responsibility of the prime contractor Thales Alenia Space (Cannes), and including Astrium (Friedrichshafen) responsible for the payload module and for system testing at spacecraft level, Thales Alenia Space (Turin) responsible for the service module, and Astrium (Toulouse) responsible for the telescope, with in excess of a hundred subcontractors.

References

Balestra, I., Mainieri, V., Popesso, P., et al. 2010, A&A, 512, A12
Blanc, G. A., Adams, J. J., Gebhardt, K., et al. 2011, ApJ, 736, 31
Bond, N. A., Gawiser, E., Gronwall, C., et al. 2009, ApJ, 705, 639
Bond, N., Gawiser, E., Guaita, L., et al. 2011, ApJ, submitted [arXiv:1104.2880]
Bongiovanni, É., Oteo, I., Cepa, J., et al. 2010, A&A, 519, L4
Bruzual, G., & Charlot, S. 2003, MNRAS, 344, 1000
Buat, V., Iglesias-Páramo, J., Seibert, M., et al. 2005, ApJ, 619, L51
Calzetti, D., Armus, L., Bohlin, R. C., et al. 2000, ApJ, 533, 682
Chapman, S. C., Blain, A. W., Smail, I., & Ivison, R. J. 2005, ApJ, 622, 772
Chary, R., & Elbaz, D. 2001, ApJ, 556, 562
Cowie, L. L., & Hu, E. M. 1998, AJ, 115, 1319
Cowie, L. L., Barger, A. J., & Hu, E. M. 2010, ApJ, 711, 928
Cowie, L. L., Barger, A. J., & Hu, E. M. 2011, ApJ, 738, 136
Deharveng, J., Small, T., Barlow, T. A., et al. 2008, ApJ, 680, 1072
Elbaz, D., Hwang, H. S., Magnelli, B., et al. 2010, A&A, 518, L29
Elbaz, D., Dickinson, M., Hwang, H. S., et al. 2011, A&A, 533, A119
Elmegreen, B. G., Elmegreen, D. M., Fernandez, M. X., & Lemonias, J. J. 2009, ApJ, 692, 12
Feldmann, R., Carollo, C. M., Porciani, C., et al. 2006, MNRAS, 372, 565
Finkelstein, S. L., Rhoads, J. E., Malhotra, S., Grogin, N., & Wang, J. 2008, ApJ, 678, 655
Finkelstein, S. L., Cohen, S. H., Malhotra, S., & Rhoads, J. E. 2009a, ApJ, 700, 276
Finkelstein, S. L., Rhoads, J. E., Malhotra, S., & Grogin, N. 2009b, ApJ, 691, 465
Finkelstein, S. L., Cohen, S. H., Moustakas, J., et al. 2011, ApJ, 733, 117
Gawiser, E., van Dokkum, P. G., Gronwall, C., et al. 2006, ApJ, 642, L13
Gawiser, E., Francke, H., Lai, K., et al. 2007, ApJ, 671, 278
Grazian, A., Fontana, A., de Santis, C., et al. 2006, A&A, 449, 951
Gronwall, C., Ciardullo, R., Hickey, T., et al. 2007, ApJ, 667, 79
Guaita, L., Gawiser, E., Padilla, N., et al. 2010, ApJ, 714, 255
Guaita, L., Acquaviva, V., Padilla, N., et al. 2011, ApJ, 733, 114
Hogg, D. W., Cohen, J. G., Blandford, R., & Pahre, M. A. 1998, ApJ, 504, 622
Hopkins, A. M. 2004, ApJ, 615, 209
Hopkins, A. M., & Beacom, J. F. 2006, ApJ, 651, 142
Kennicutt, Jr., R. C. 1998, ARA&A, 36, 189
Kornei, K. A., Shapley, A. E., Erb, D. K., et al. 2010, ApJ, 711, 693
Lai, K., Huang, J., Fazio, G., et al. 2008, ApJ, 674, 70
Le Floc'h, E., Papovich, C., Dole, H., et al. 2005, ApJ, 632, 169
Lutz, D., Poglitsch, A., Altieri, B., et al. 2011, A&A, 532, A90
Madau, P. 1995, ApJ, 441, 18
Murayama, T., Taniguchi, Y., Scoville, N. Z., et al. 2007, ApJS, 172, 523
Neufeld, D. A. 1991, ApJ, 370, L85
Nilsson, K. K., & Møller, P. 2009, A&A, 508, L21
Nilsson, K. K., Møller, P., Möller, O., et al. 2007, A&A, 471, 71
Nilsson, K. K., Tapken, C., Møller, P., et al. 2009, A&A, 498, 13
Nilsson, K. K., Östlin, G., Møller, P., et al. 2011, A&A, 529, A9
Nordon, R., Lutz, D., Shao, L., et al. 2010, A&A, 518, L24
Oke, J. B., & Gunn, J. E. 1983, ApJ, 266, 713
Ono, Y., Ouchi, M., Shimasaku, K., et al. 2010, MNRAS, 402, 1580
Oteo, I., Bongiovanni, A., Pérez García, A. M., et al. 2011, ApJ, 735, L15
Oteo, I., Bongiovanni, A., Pérez García, A. M., et al. 2012, ApJ, in press [arXiv:1204.0782v1]
Ouchi, M., Shimasaku, K., Akiyama, M., et al. 2008, ApJS, 176, 301

Ouchi, M., Shimasaku, K., Furusawa, H., et al. 2010, ApJ, 723, 869
Peng, C. Y., Ho, L. C., Impey, C. D., & Rix, H. 2010, AJ, 139, 2097
Pentericci, L., Grazian, A., Fontana, A., et al. 2007, A&A, 471, 433
Pentericci, L., Grazian, A., Scarlata, C., et al. 2010, A&A, 514, A64
Pérez-González, P. G., Rieke, G. H., Egami, E., et al. 2005, ApJ, 630, 82
Pilbratt, G. L., Riedinger, J. R., Passvogel, T., et al. 2010, A&A, 518, L1
Pirzkal, N., Malhotra, S., Rhoads, J. E., & Xu, C. 2007, ApJ, 667, 49
Poglitsch, A., Waelkens, C., Geis, N., et al. 2010, A&A, 518, L2
Popesso, P., Dickinson, M., Nonino, M., et al. 2009, A&A, 494, 443
Reddy, N. A., Erb, D. K., Pettini, M., Steidel, C. C., & Shapley, A. E. 2010, ApJ, 712, 1070
Rhoads, J. E., Malhotra, S., Dey, A., et al. 2000, ApJ, 545, L85
Salpeter, E. E. 1955, ApJ, 121, 161
Santini, P., Fontana, A., Grazian, A., et al. 2009, A&A, 504, 751
Sersic, J. L. 1968, Atlas de galaxias australes (Cordoba, Argentina: Observatorio Astronomico)
Shioya, Y., Taniguchi, Y., Sasaki, S. S., et al. 2009, ApJ, 696, 546
Wuyts, S., Förster Schreiber, N. M., Lutz, D., et al. 2011, ApJ, 738, 106

Pages 11 to 19 are available in the electronic edition of the journal at http://www.aanda.org

Appendix A: Physical properties of the Lyα emitting galaxies studied

Table A.1. Physical properties of our sample of 56 galaxies at $2.0 \lesssim z \lesssim 3.5$ as derived from SED fitting with BC03 templates.

Name	Redshift	Age [Myr]	$E_s(B-V)$[BC03]	$SFR_{\rm UV,uncorrected}$ [$M_\odot$ yr^{-1}]	$\log(M_*/M_\odot)$
GOODS_LRb_dec06_3_q2_33_2	2.0214	29 ± 34	0.25 ± 0.07	6.7	8.2
GOODS_LRb_002_q3_86_1	2.0526	21 ± 6	0.30 ± 0.05	17.0	8.5
GOODS_LRb_002_1_q3_88_1	2.0600	47 ± 8	0.15 ± 0.05	4.8	8.3
GOODS_LRb_002_1_q4_79_1	2.1449	25 ± 6	0.15 ± 0.23	20.0	8.6
GOODS_LRb_001_q3_24_2	2.1659	15 ± 6	0.20 ± 0.06	9.1	8.1
GOODS_LRb_dec06_1_q2_41_1	2.1809	541 ± 6	0.10 ± 0.05	2.3	9.1
GOODS_LRb_dec06_1_q4_15_2	2.2128	121 ± 17	0.10 ± 0.05	20.4	9.3
GOODS_LRb_001_q2_7_1	2.2158	383 ± 10	0.15 ± 0.05	2.5	8.9
GOODS_LRb_dec06_1_q2_48_1	2.2991	11 ± 32	0.20 ± 0.09	3.2	7.5
GOODS_LRb_002_1_q1_16_2	2.3115	5 ± 5	0.25 ± 0.19	15.9	7.9
GOODS_LRb_002_1_q4_29_1	2.3143	11 ± 24	0.30 ± 0.06	9.7	8.0
GOODS_LRb_dec06_3_q3_51_1	2.3166	305 ± 9	0.15 ± 0.05	6.2	9.2
GOODS_LRb_dec06_3_q2_22_1	2.3170	31 ± 21	0.15 ± 0.05	17.3	8.7
GOODS_LRb_dec06_1_q1_11_3	2.3200	55 ± 22	0.20 ± 0.06	27.5	9.1
GOODS_LRb_dec06_1_q1_15_1	2.4000	121 ± 5	0.00 ± 0.05	5.4	8.8
GOODS_LRb_001_q1_8_1	2.4284	1750 ± 13	0.20 ± 0.14	19.6	10.5
GOODS_LRb_002_1_q4_69_1	2.4304	33 ± 32	0.25 ± 0.05	13.1	8.6
GOODS_LRb_dec06_3_q3_53_3	2.4645	39 ± 5	0.10 ± 0.05	4.5	8.2
GOODS_LRb_dec06_1_q3_60_1	2.4834	13 ± 6	0.15 ± 0.05	10.9	8.1
GOODS_LRb_002_1_q4_1_1	2.4835	121 ± 7	0.05 ± 0.05	22.1	9.4
GOODS_LRb_dec06_3_q3_60_1	2.5144	9 ± 18	0.40 ± 0.05	11.9	8.0
GOODS_LRb_002_1_q1_26_1	2.5600	1 ± 5	0.40 ± 0.16	13.4	7.1
GOODS_LRb_001_q3_47_2	2.5641	383 ± 9	0.00 ± 0.05	4.8	9.2
GOODS_LRb_001_q2_14_1	2.5671	215 ± 9	0.15 ± 0.05	9.2	9.2
GOODS_LRb_002_1_q4_32_1	2.6159	305 ± 8	0.00 ± 0.05	7.6	9.3
GOODS_LRb_002_1_q1_62_1	2.6191	341 ± 8	0.00 ± 0.05	7.8	9.4
GOODS_LRb_001_q2_37_1	2.6489	77 ± 10	0.10 ± 0.05	12.5	8.9
GOODS_LRb_dec06_1_q3_39_2	2.6607	5 ± 6	0.25 ± 0.07	11.4	7.7
GOODS_LRb_dec06_1_q3_32_1	2.6692	153 ± 13	0.10 ± 0.05	8.0	9.0
GOODS_LRb_001_q3_69_1	2.6796	7 ± 4	0.10 ± 0.05	4.6	7.5
GOODS_LRb_001_q2_31_1	2.6914	1210 ± 10	0.10 ± 0.05	9.1	10.0
GOODS_LRb_001_q3_60_1	2.6933	171 ± 11	0.20 ± 0.05	7.2	9.0
GOODS_LRb_dec06_2_q3_44_1	2.7034	305 ± 14	0.15 ± 0.05	16.0	9.6
GOODS_LRb_001_q2_39_1	2.7184	101 ± 6	0.05 ± 0.05	6.4	8.8
GOODS_LRb_001_q2_44_2	2.7237	3 ± 2	0.30 ± 0.19	104.6	8.4
GOODS_LRb_dec06_1_q4_5_2	2.7269	3 ± 5	0.30 ± 0.08	10.7	7.5
GOODS_LRb_001_q3_9_1	2.8079	27 ± 10	0.30 ± 0.05	10.7	8.4
GOODS_LRb_001_q2_9_1	2.8121	61 ± 9	0.15 ± 0.05	25.6	9.1
GOODS_LRb_dec06_2_q3_51_1	2.8130	101 ± 10	0.10 ± 0.05	9.1	8.9
GOODS_LRb_001_q4_22_1	2.9659	429 ± 3	0.00 ± 0.05	3.2	9.1
GOODS_LRb_001_q2_13_1	3.0058	5 ± 2	0.25 ± 0.19	119.2	8.7
GOODS_LRb_001_q3_48_1	3.0201	9 ± 6	0.30 ± 0.10	16.4	8.1
GOODS_LRb_001_q3_89_2	3.0300	121 ± 11	0.15 ± 0.05	10.6	9.1
GOODS_LRb_dec06_1_q4_7_1	3.0872	21 ± 27	0.20 ± 0.07	12.3	8.4
GOODS_LRb_002_1_q1_52_2	3.0920	39 ± 8	0.10 ± 0.05	3.9	8.1
GOODS_LRb_dec06_1_q4_45_3	3.1316	121 ± 9	0.10 ± 0.05	6.7	8.9
GOODS_LRb_001_q2_84_1	3.1677	9 ± 6	0.15 ± 0.05	12.1	8.0
GOODS_LRb_001_q3_84_1	3.1733	763 ± 10	0.05 ± 0.05	6.4	9.6
GOODS_LRb_dec06_3_q3_42_1	3.2000	193 ± 18	0.10 ± 0.05	6.8	9.1
GOODS_LRb_dec06_1_q3_41_1	3.2078	69 ± 10	0.10 ± 0.05	27.0	9.2
GOODS_LRb_dec06_3_q3_65_2	3.2293	57 ± 16	0.20 ± 0.05	21.5	9.0
GOODS_LRb_001_q3_71_2	3.2479	87 ± 25	0.15 ± 0.06	9.3	8.9
GOODS_LRb_002_1_q1_33_1	3.3565	5 ± 4	0.20 ± 0.05	8.7	7.6
GOODS_LRb_001_q2_30_1	3.3850	153 ± 6	0.05 ± 0.05	8.1	9.0
GOODS_LRb_002_1_q2_71_1	3.4724	25 ± 9	0.15 ± 0.05	21.5	8.7
GOODS_LRb_dec06_3_q3_31_1	3.5400	37 ± 6	0.10 ± 0.05	4.6	8.2

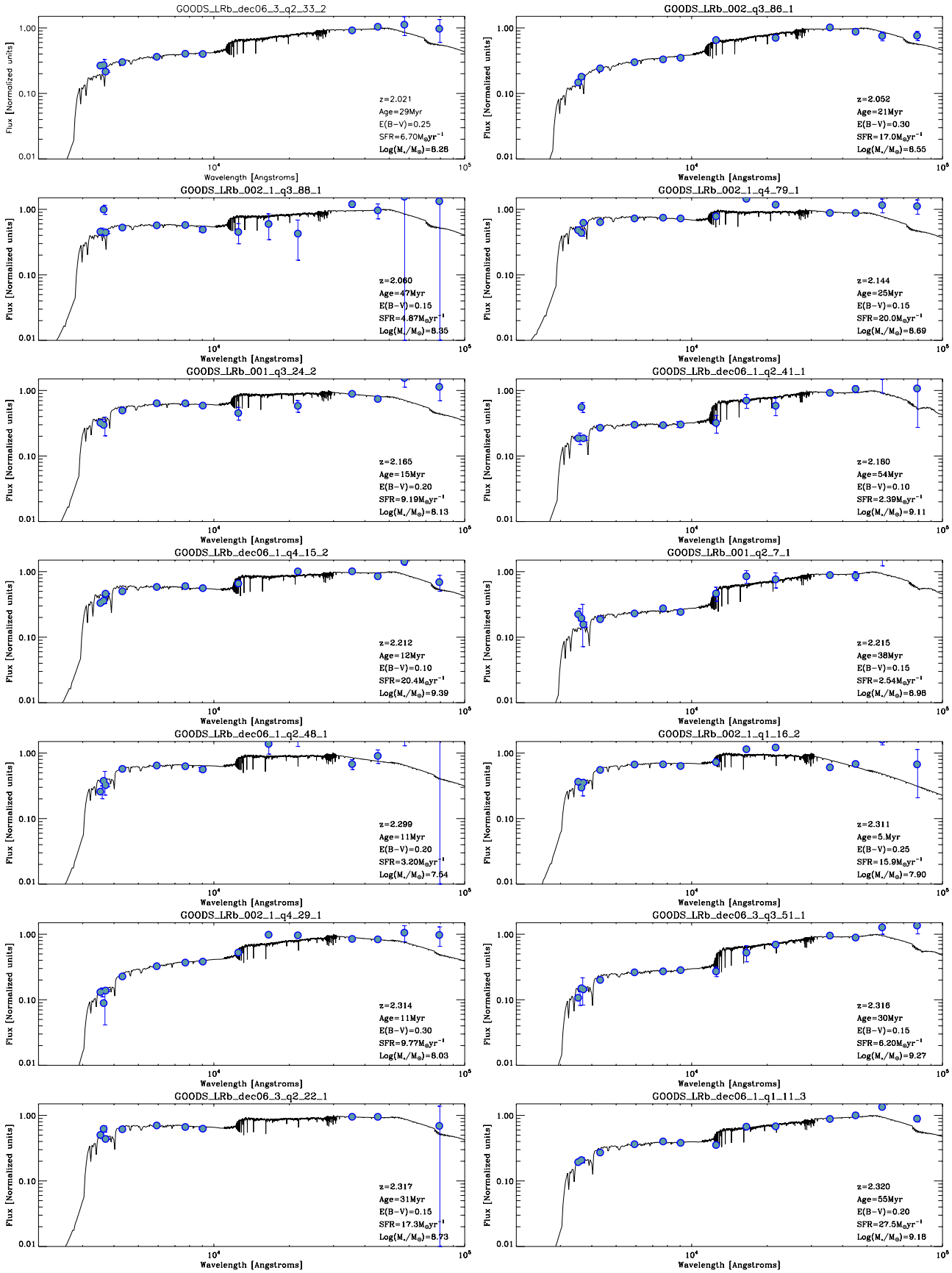

Fig. A.1. BC03 templates which best fit the observed SED of the 56 galaxies studied.

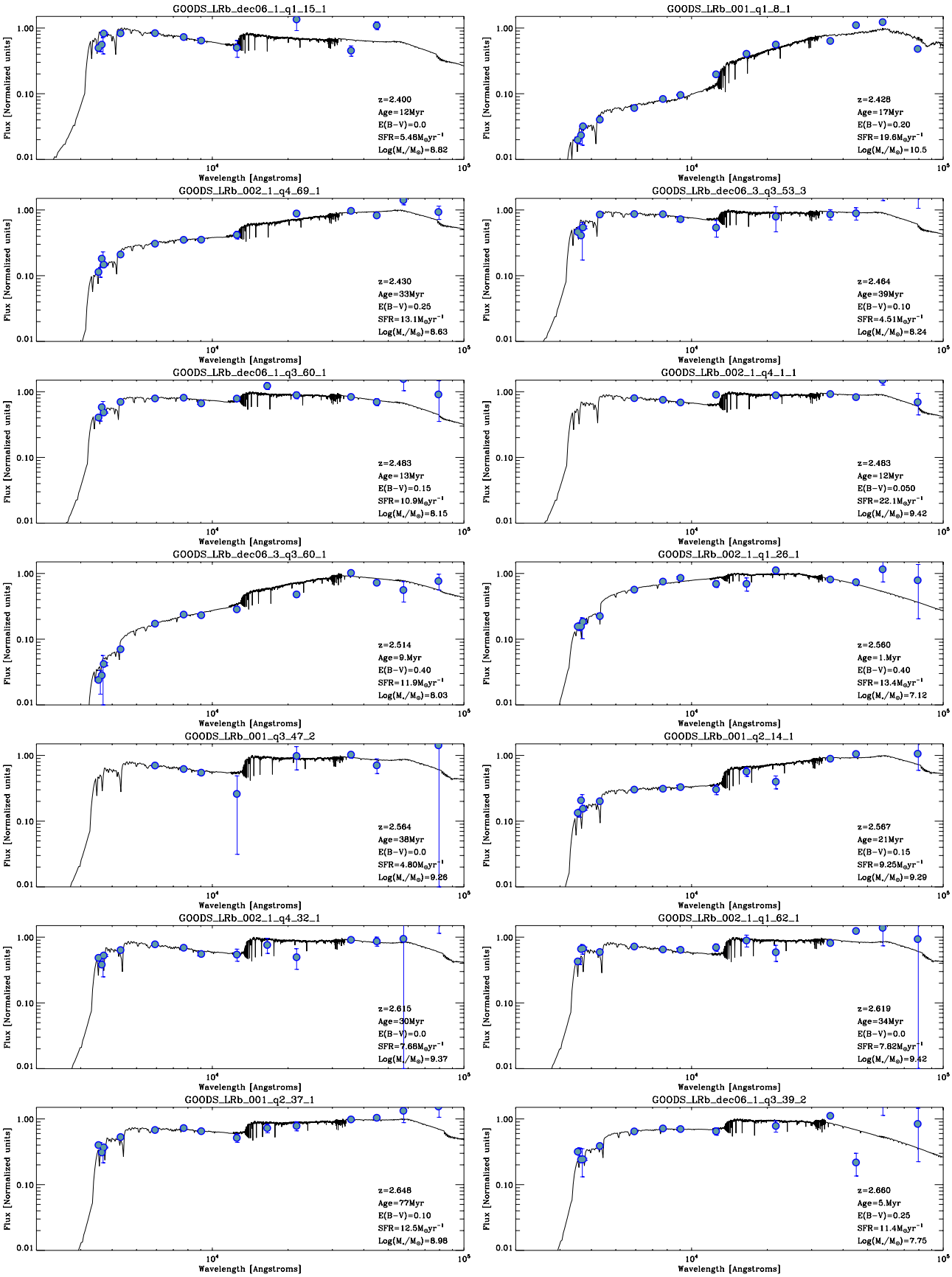

Fig. A.1. continued.

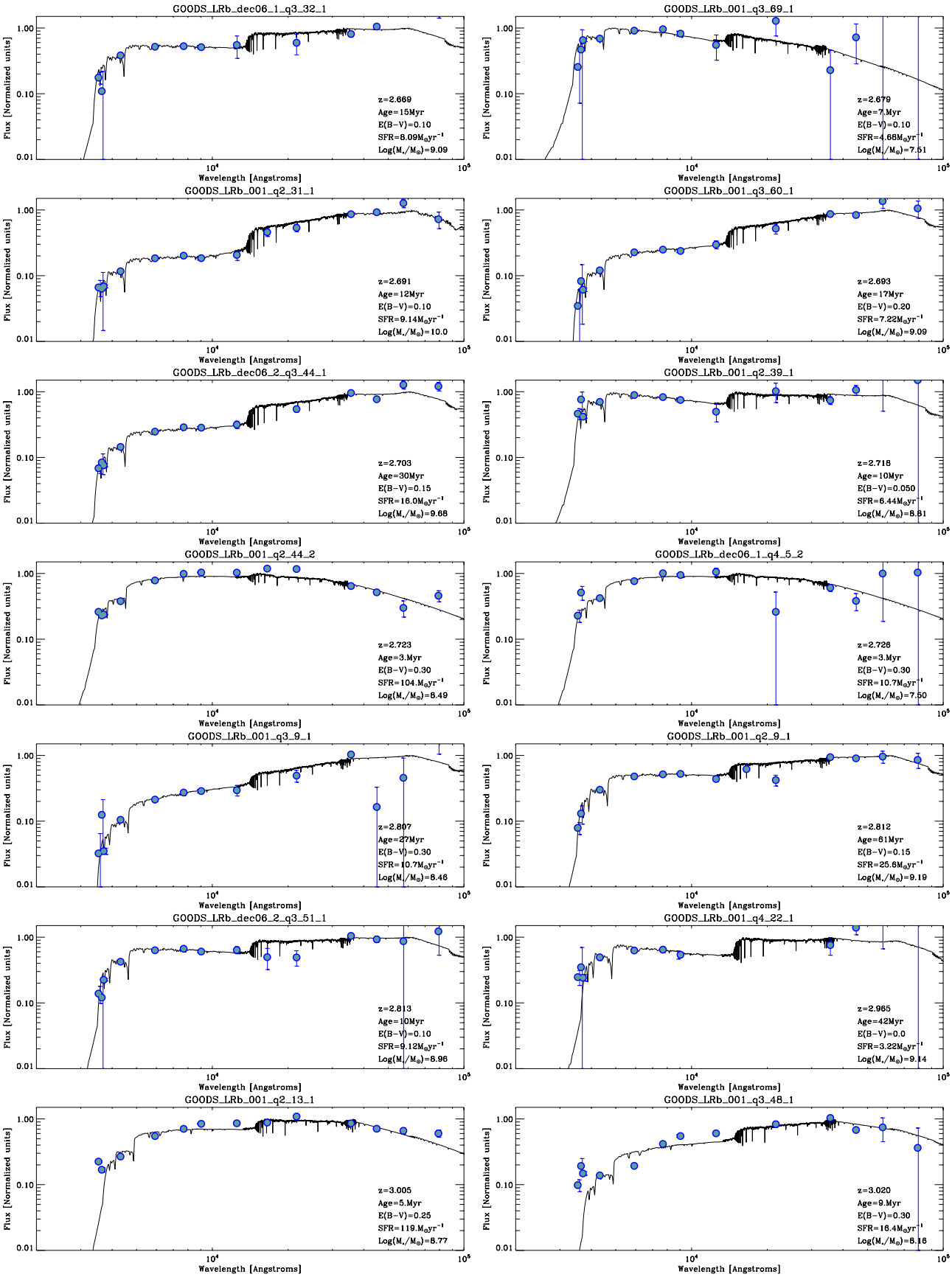

Fig. A.1. continued.

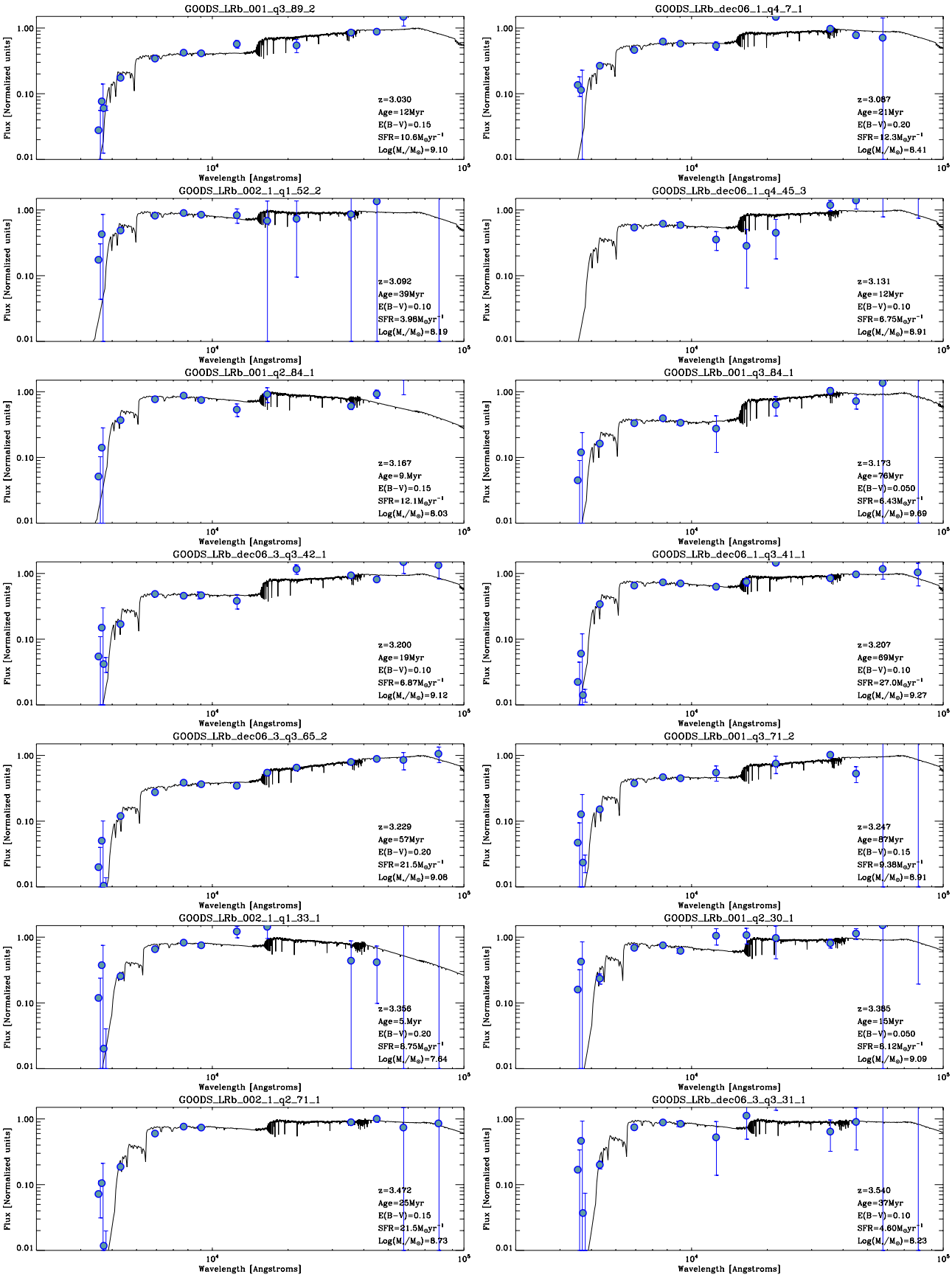

Fig. A.1. continued.

(a) GOODS_LRb_dec06_3_q2_33_2 (b) GOODS_LRb_002_q3_86_1

(c) GOODS_LRb_002_1_q3_88_1 (d) GOODS_LRb_002_1_q4_79_1

(e) GOODS_LRb_001_q3_24_2 (f) GOODS_LRb_dec06_1_q2_41_1

(g) GOODS_LRb_dec06_1_q4_15_2 (h) GOODS_LRb_001_q2_7_1

(i) GOODS_LRb_dec06_1_q2_48_1 (j) GOODS_LRb_002_1_q1_16_2

(k) GOODS_LRb_002_1_q4_29_1 (l) GOODS_LRb_dec06_3_q3_51_1

(m) GOODS_LRb_dec06_3_q2_22_1 (n) GOODS_LRb_dec06_1_q1_11_3

(o) GOODS_LRb_dec06_1_q1_15_1 (p) GOODS_LRb_001_q1_8_1

Fig. A.2. $5' \times 5'$ ACS optical cut-outs of the galaxies in our sample. The white cut-out indicates that there is no information of that object in that photometric band.

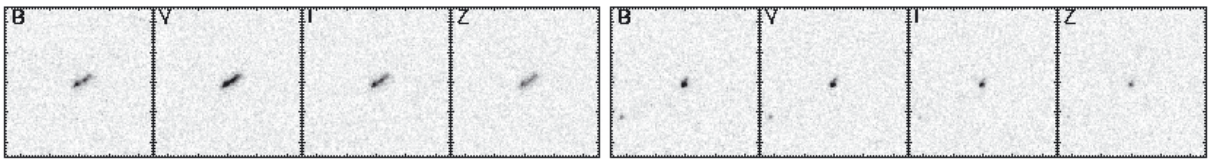

(a) GOODS_LRb_002_1_q4_69_1

(b) GOODS_LRb_dec06_3_q3_53_3

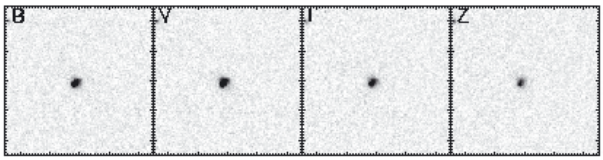

(c) GOODS_LRb_dec06_1_q3_60_1

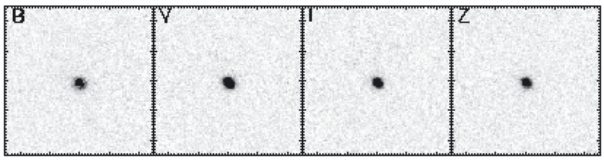

(d) GOODS_LRb_002_1_q4_1_1

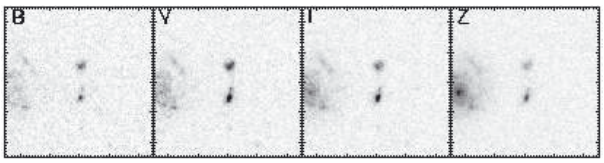

(e) GOODS_LRb_dec06_3_q3_60_1

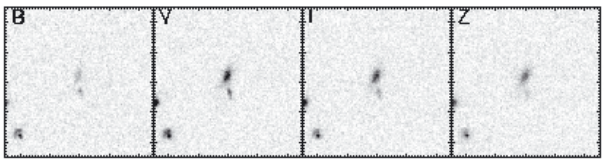

(f) GOODS_LRb_002_1_q1_26_1

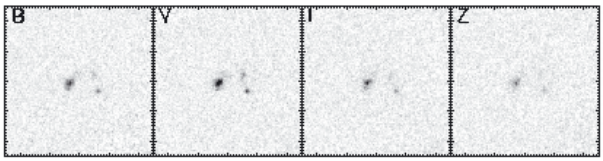

(g) GOODS_LRb_001_q3_47_2

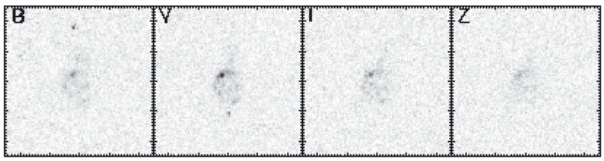

(h) GOODS_LRb_001_q2_14_1

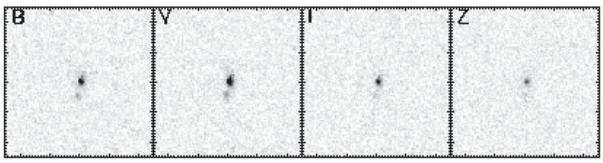

(i) GOODS_LRb_002_1_q4_32_1

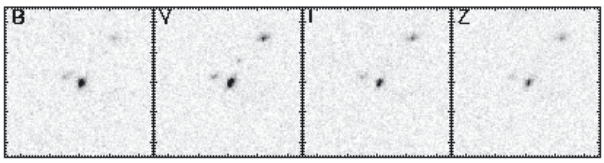

(j) GOODS_LRb_002_1_q1_62_1

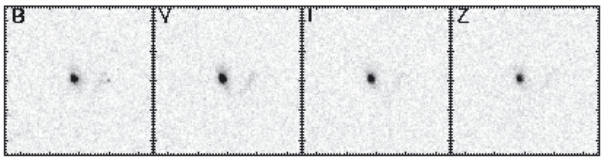

(k) GOODS_LRb_001_q2_37_1

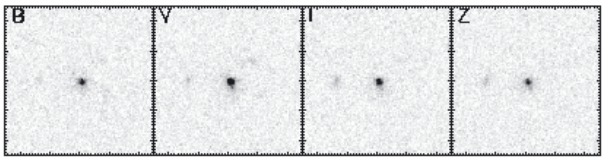

(l) GOODS_LRb_dec06_1_q3_39_2

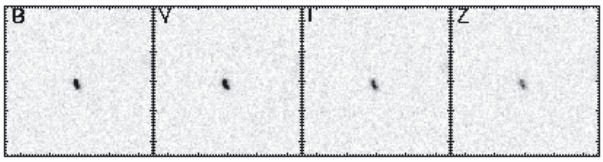

(m) GOODS_LRb_dec06_1_q3_32_1

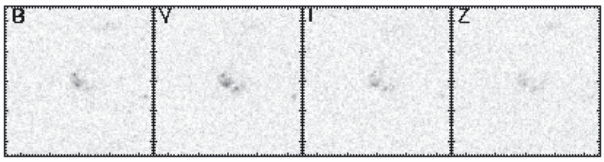

(n) GOODS_LRb_001_q3_69_1

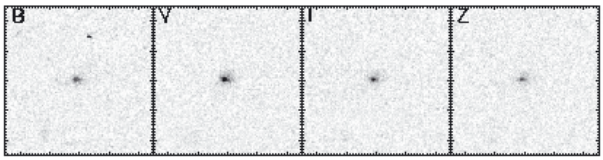

(o) GOODS_LRb_001_q2_31_1

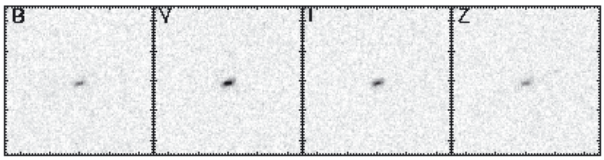

(p) GOODS_LRb_001_q3_60_1

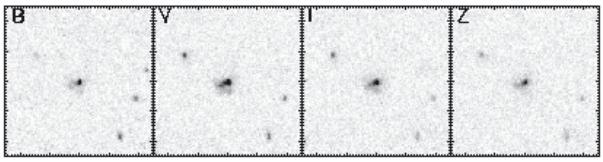

(q) GOODS_LRb_dec06_2_q3_44_1

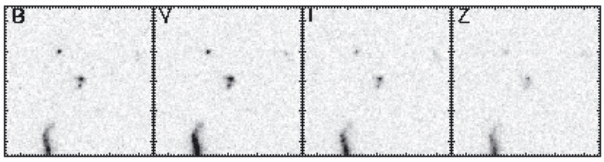

(r) GOODS_LRb_001_q2_39_1

Fig. A.2. continued.

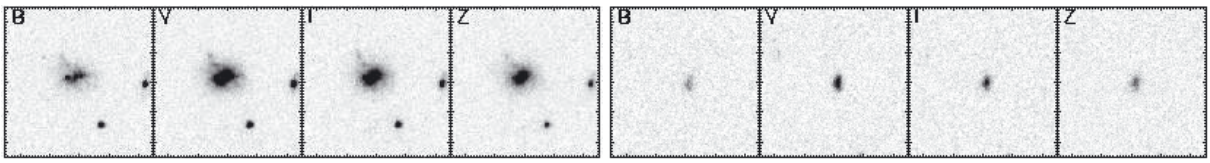

(a) GOODS_LRb_001_q2_44_2

(b) GOODS_LRb_dec06_1_q4_5_2

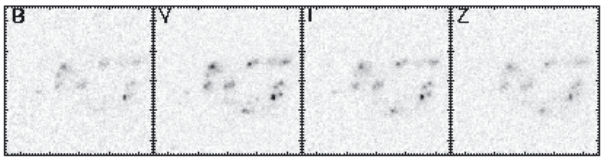

(c) GOODS_LRb_001_q3_9_1

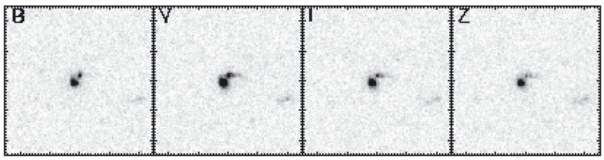

(d) GOODS_LRb_001_q2_9_1

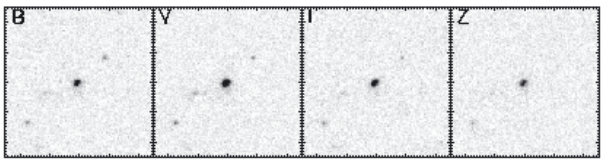

(e) GOODS_LRb_dec06_2_q3_51_1

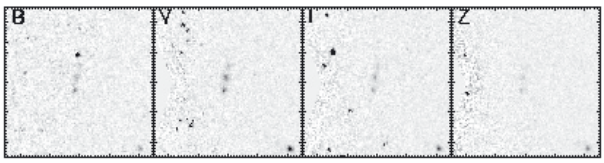

(f) GOODS_LRb_001_q4_22_1

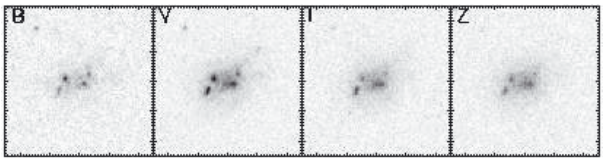

(g) GOODS_LRb_001_q2_13_1

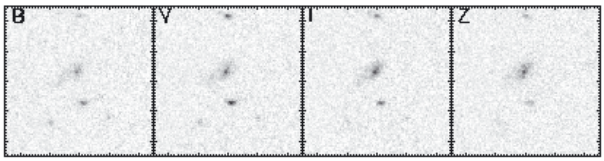

(h) GOODS_LRb_001_q3_48_1

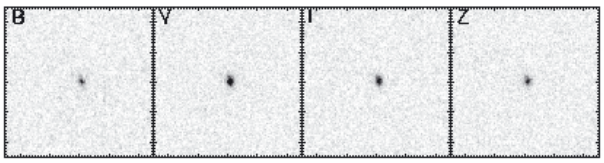

(i) GOODS_LRb_001_q3_89_2

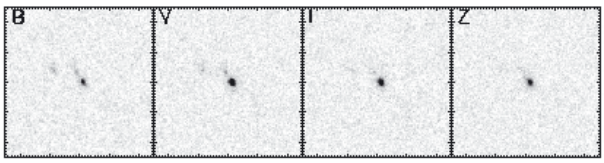

(j) GOODS_LRb_dec06_1_q4_7_1

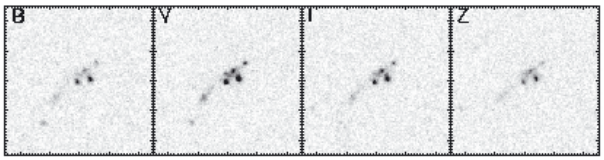

(k) GOODS_LRb_002_1_q1_52_2

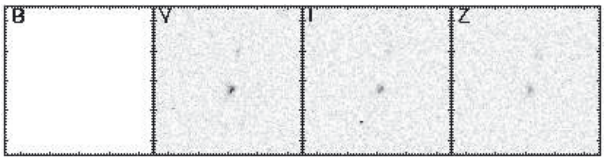

(l) GOODS_LRb_dec06_1_q4_45_3

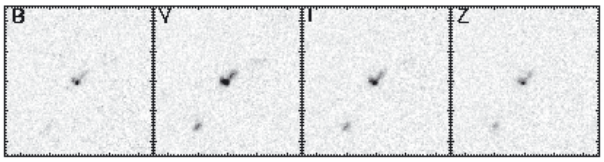

(m) GOODS_LRb_001_q2_84_1

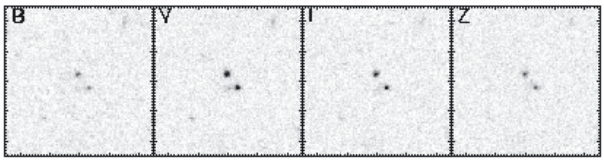

(n) GOODS_LRb_001_q3_84_1

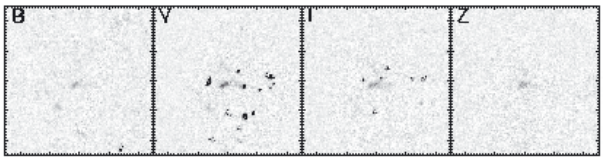

(o) GOODS_LRb_dec06_3_q3_42_1

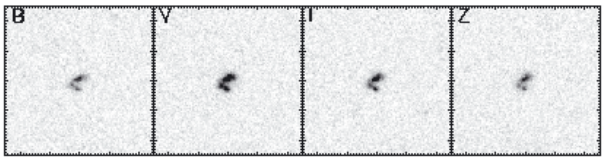

(p) GOODS_LRb_dec06_1_q3_41_1

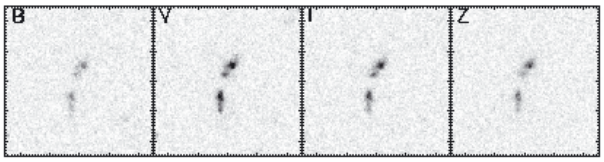

(q) GOODS_LRb_dec06_3_q3_65_2

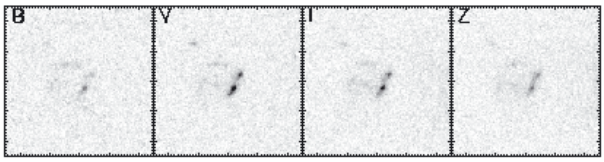

(r) GOODS_LRb_001_q3_71_2

Fig. A.2. continued.

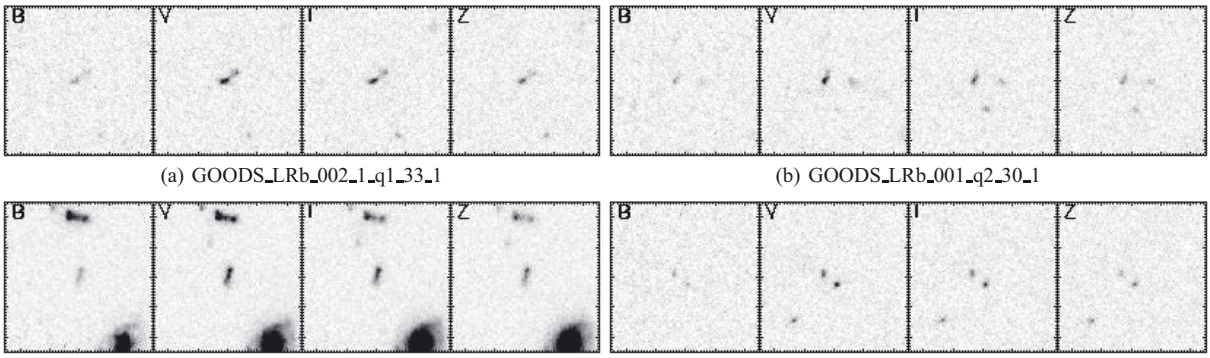

(a) GOODS_LRb_002_1_q1_33_1

(b) GOODS_LRb_001_q2_30_1

(c) GOODS_LRb_002_1_q2_71_1

(d) GOODS_LRb_dec06_3_q3_31_1

Fig. A.2. continued.